

Pixel screening based intermediate correction for blind deblurring

Meina Zhang¹ Yingying Fang² Guoxi Ni^{1*} Tieyong Zeng^{3*}

¹Institute of Applied Physics and Computational Mathematics, Beijing, China

² Imperial College London, London, United Kingdom

³The Chinese University of Hong Kong, Shatin, Hong Kong

mnzhang01@gmail.com, y.fang@imperial.ac.uk, gxni@iapcm.ac.cn, zeng@math.cuhk.edu.hk

Abstract

Blind deblurring has attracted much interest with its wide applications in reality. The blind deblurring problem is usually solved by estimating the intermediate kernel and the intermediate image alternatively, which will finally converge to the blurring kernel of the observed image. Numerous works have been proposed to obtain intermediate images with fewer undesirable artifacts by designing delicate regularization on the latent solution. However, these methods still fail while dealing with images containing saturations and large blurs. To address this problem, we propose an intermediate image correction method which utilizes Bayes posterior estimation to screen through the intermediate image and exclude those unfavorable pixels to reduce their influence for kernel estimation. Extensive experiments have proved that the proposed method can effectively improve the accuracy of the final derived kernel against the state-of-the-art methods on benchmark datasets by both quantitative and qualitative comparisons.

1. Introduction

Blurry images can easily occur when the photography equipment suffers from slight movement. As the target scene is usually irreproducible, how to efficiently recover the contents from the blurry images has attracted much attention. Mathematically, the degradation of a blurry image is usually modeled as a convolution of a latent sharp image \mathcal{U} with a spatial invariant kernel \mathcal{K} which represents the moving trajectory of the equipment. Hence, we have:

$$\mathcal{B} = \mathcal{K} * \mathcal{U} + \varepsilon, \quad (1)$$

where \mathcal{B} denotes the observed blurry image, $*$ denotes the convolution operator and ε is additive white Gaussian noise (AWGN) which frequently appears in the real world.

*Corresponding authors

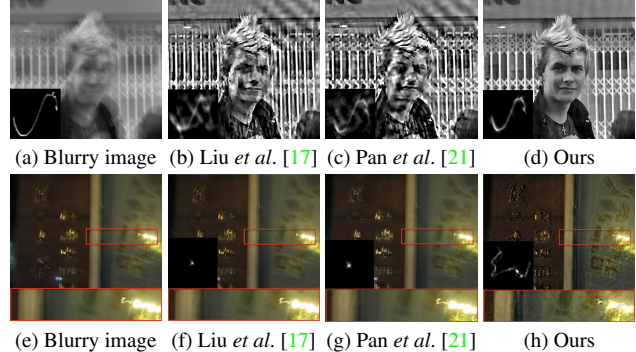


Figure 1. The comparison of the estimated kernel and deblurred results on two challenging cases. The first line shows the results of an image blurred by a large kernel; the second line shows the results of an image captured in the real world with saturation points. Note that the kernel in the bottom left of the blurry image is used for synthetic while others are estimated. In these cases, our method estimates the kernel accurately while other methods get noisy kernels or fail to estimate any shape. (Zoom in for better viewing).

As both the blurring kernel \mathcal{K} and the sharp image \mathcal{U} are unknown, a common strategy is to update them in an alternative way. Starting from an initial guess \mathcal{K}^0 , for any iteration k , we can iterate as follows:

$$\begin{aligned} \mathcal{U}^{k+1} &= \underset{\mathcal{U}}{\operatorname{argmin}} \left\{ \|\mathcal{B} - \mathcal{K}^k * \mathcal{U}\|_2^2 + \rho_U(\mathcal{U}) \right\}, \\ \mathcal{K}^{k+1} &= \underset{\mathcal{K}}{\operatorname{argmin}} \left\{ \|\mathcal{B} - \mathcal{K} * \mathcal{U}^{k+1}\|_2^2 + \rho_K(\mathcal{K}) \right\}, \end{aligned} \quad (2)$$

where $\rho_U(\mathcal{U})$ and $\rho_K(\mathcal{K})$ are regularizers designed by some suitable priors on the latent desired image and kernel. The procedure in Eq. (2), which is aimed to produce the final estimated kernel, is referred to as blind deblurring [1, 9, 17, 22, 24, 37]. Following it, the final deblurred image is derived using a non-blind deblurring model [5, 33], which takes the kernel returned by the blind deblurring and the given kernel \mathcal{K} plays a great role on the final result. In this regard, our goal is to improve the accuracy of the kernel derived by the blind deblurring procedure Eq. (2) to enhance the final

deblurred result.

Many excellent works have been investigated to design the formulas of $\rho_U(\mathcal{U})$ and $\rho_K(\mathcal{K})$ in Eq. (2) to improve the kernel estimation accuracy [4, 11, 17, 24, 32, 34–36]. Among them, significant efforts have been made to drive the intermediate image closer to the sharp image with less artifacts, so as to use it to get an ideal kernel. Specifically, Pan *et al.* [24] proposed a generic regularization on the dark channel of the latent sharp image, and reached leading performance. Furthermore, Liu *et al.* [17] proposed a surface-aware function smoothing the artifacts presented in the intermediate images and produced a more exact kernel.

Despite their effectiveness in many cases, their performance degrades inevitably while dealing with the blurry images with large blurs or saturations. There are two major problems that easily occur in these challenging cases. As illustrated in Fig. 1 (a)-(c), while estimating the large kernel from images, the methods [17, 21] generate rather noisy kernels, with which the final deblurred results contain serious ringing artifacts. In the other case illustrated in Fig. 1 (e)-(g), when the iteration Eq. (2) increases, the estimated intermediate image remains as the blurry input and the estimated kernel remains as the nearly identity input, which means they fall into the local minimizer of the non-convex blind deblurring problem.

To solve these problems, we propose a pixel screening method to further correct the intermediate image, believing that a good intermediate image facilitates to estimate a better kernel. From our observation of the conventional deblurring iterations, whose details are illustrated in Fig. 2, we find that there exists a certain number of pixels in the intermediate images that does not satisfy the model Eq. (1) with the given estimated kernel. Moreover, we can see from Fig. 2 that these pixels are useless and even harmful for kernel estimation. As these unnecessary structures have adverse influence on kernel estimation in the next step, we are motivated to utilize a random operator to distinguish them from the normal pixels. Hence, we propose a pixel screening map which calculates the weight for each pixel to decide whether it conforms Eq. (1). Those undesirable pixels will then be removed from the intermediate image for the subsequent kernel estimation step. In this way, we effectively relieve the influence of those unfavorable structures and obtain the more accurate blurring kernels.

The main contributions of this work are summarized as follows: (1) we initially find that the linear degradation model helps in locating the unnecessary structures in the intermediate images; (2) we propose a new and effective blind deblurring model by correcting the intermediate image with the proposed pixel screening strategy, which proves to prompt the kernel away from the initial location and facilitate a more accurate kernel estimation; (3) we demonstrate the superiority of our method on the common

benchmark datasets [12, 14, 16], and the specific challenging benchmarks with large blur kernels and saturation as well as the real-world images by comparing with the state-of-the-art both quantitatively and qualitatively.

2. Related Works

Significant advances have been made in blind deblurring tasks in the last decades. For instance, Cho and Lee [4] extracted edge information from the latent image and suppressed the artifacts by removing the noise of intermediate image to optimize the kernel estimation. Xu and Jia [34] proposed a criterion to measure the usefulness of edges for kernel estimation. Furthermore, Yang *et al.* [38] built an adaptive edge selection algorithm based on the assumption that a good intermediate image estimation is not necessarily the one closest to the latent image.

While these works improve the accuracy of the kernel estimation by selecting the salient information from the intermediate images, another branch of works resort to design a preciser prior to regularize the latent image to be a sharper intermediate image with less artifacts. For example, Xu *et al.* [35] considered the sparsity prior of the sharp image gradients and proposed to minimize the approximating L_0 norm of the gradient to enforce the sparsity on image gradient. Pan *et al.* [22] further applied an extra L_0 -sparsity on the image intensity to reduce the unnecessary structures. Beyond the edge information, Pan *et al.* [24] proposed the sparsity on the dark channel based on the observation that sharp images are sparser in the dark channel than the blurry images. To preserve more details in the intermediate image, Liu *et al.* [18] presented a super-Gaussian field model to capture more complicated structures in images. Chen *et al.* [1] considered a local maximum gradient prior for mining more information from blurry images and got intermediate images with more textures. Different from them, Liu *et al.* [17] observed the intrinsic geometry structure of intermediate images and proposed a surface-aware prior with the aim of inhibiting the undesirable artifacts of the intermediate while reserving the sharp edges in the meanwhile.

Recently, deep learning (DL)-based methods have also developed in blind deblurring [27, 29, 30, 39]. Ren *et al.* [27] utilized a fully connected neural network and a CNN to approximate the blur kernel and latent image, respectively. Tran *et al.* [29] trained a residual net to extract blurring kernel and a U-net to simulate the blurring process. However, these DL-based methods heavily rely on the training data and easily fail to infer the kernels from the images with kernels that are not included in the training process. For this reason, in this paper we focus on improving the iterative blind deblurring method, which is more stable and precise.

In this work, we will also propose a pixel screening method to locate the disadvantageous pixels existing in the intermediate images during the blind deblurring iterations

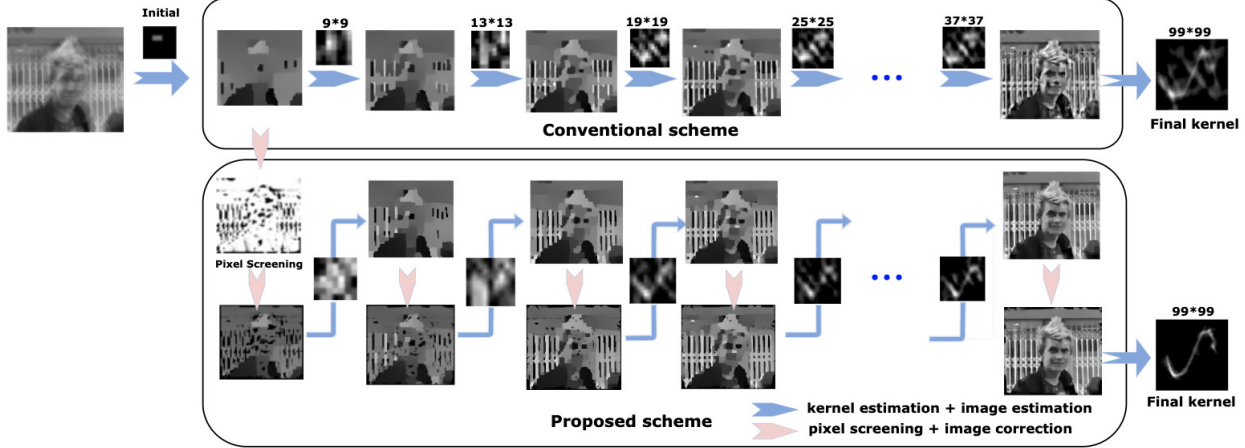


Figure 2. Overview of the proposed method. The top block shows the intermediate results using the strategy of Liu *et al.* [17], the bottom block shows intermediate results of our method. We can see that the corrected intermediate images in the first few steps are more sharp, which prompts the kernel to leave the identity map. In the lateral steps, the correction strategy significantly suppresses the artifacts and modifies the intermediate image closer to the latent image.

based on the confidence map introduced in [5]. To improve the kernel accuracy, we apply it after each image estimation step to exclude those undesirable pixels which may harm the kernel estimation.

3. Proposed method

In this section, we will first introduce the proposed pixel screening strategy, after which we will present the proposed intermediate image correction model as well as the alternating numerical scheme to solve it.

3.1. Pixel screening method

Our key idea is that the recovered intermediate image \mathcal{U} and the estimated kernel \mathcal{K} in the blind deblurring model are not always conforming to the ideal condition in Eq. (1), which may lead to the deviation of the intermediate kernel and image in the iterative process. In order to prevent these pixels from adversely affecting the blur kernel estimation, we propose a pixel screening strategy to exclude the disadvantageous pixels existing in the intermediate images during the blind deblurring iterations before estimating the kernel. Applying the calculation of the confidence map introduced in [5], we define the probability of each pixel being a non-deviated point in the intermediate image given the intermediate image and kernel as:

$$P_{ij}^{k+1} = \mathcal{P}(\mathcal{Z}_{ij}^{k+1} = 1 | \mathcal{B}_{ij}, \mathcal{K}^k, \mathcal{U}^{k+1}), \quad (3)$$

where P_{ij}^{k+1} is the posterior distribution under \mathcal{U}^{k+1} and \mathcal{K}^k . Here, we introduce a variable \mathcal{Z}^{k+1} as the pixel indicator to show whether the pixels in the $(k+1)$ -th intermediate image satisfy the ideal assumption Eq. (1). Denoting Ω as

the whole image space, I^c as the space where pixels are not compatible to Eq. (1) and $I = \Omega / I^c$ as the pixels that satisfy the Eq. (1), the variable \mathcal{Z} is explicitly defined as:

$$\mathcal{Z}(\mathcal{U}_{ij}) = \mathbf{1}_I(\mathcal{U}_{ij}), \quad (4)$$

where $\mathbf{1}$ is an indicator function in a discrete image for classification. The Bayes' theorem can then transform Eq. (3) into

$$\begin{aligned} & \mathcal{P}(\mathcal{Z}_{ij}^{k+1} = 1 | \mathcal{B}_{ij}, \mathcal{K}^k, \mathcal{U}^{k+1}) \\ &= \frac{\mathcal{P}(\mathcal{B}_{ij} | \mathcal{Z}_{ij}^{k+1} = 1, \mathcal{K}^k, \mathcal{U}^{k+1}) \mathcal{P}(\mathcal{Z}_{ij}^{k+1} = 1 | \mathcal{K}^k, \mathcal{U}^{k+1})}{\mathcal{P}(\mathcal{B}_{ij} | \mathcal{K}^k, \mathcal{U}^{k+1})} \\ &= \frac{\mathcal{P}(\mathcal{B}_{ij} | \mathcal{Z}_{ij}^{k+1} = 1, \mathcal{K}^k, \mathcal{U}^{k+1}) \mathcal{P}(\mathcal{Z}_{ij}^{k+1} = 1 | \mathcal{K}^k, \mathcal{U}^{k+1})}{\sum_{\mathcal{Z}_{ij}=0}^1 \mathcal{P}(\mathcal{B}_{ij} | \mathcal{Z}_{ij}^{k+1}, \mathcal{K}^k, \mathcal{U}^{k+1}) \mathcal{P}(\mathcal{Z}_{ij}^{k+1} | \mathcal{K}^k, \mathcal{U}^{k+1})}. \end{aligned} \quad (5)$$

According to the assumption in Eq. (1) where $\varepsilon \sim \mathcal{N}(0, \sigma^2)$, we have the probability

$$\mathcal{P}(\mathcal{B}_{ij} | \mathcal{Z}_{ij}^{k+1} = 1, \mathcal{K}^k, \mathcal{U}^{k+1}) = \mathcal{N}((\mathcal{K}^k * \mathcal{U}^{k+1})_{ij}, \sigma^2), \quad (6)$$

For the other case $\mathcal{Z}_{ij} = 0$, which means the pixel is regarded as a deviated points whose posterior distribution does not obey Gaussian distribution, we approximate $\mathcal{P}(\mathcal{B}_{ij} | \mathcal{Z}_{ij}^{k+1} = 0, \mathcal{K}^k, \mathcal{U}^{k+1})$ by a uniform distribution defined as

$$\mathcal{P}(\mathcal{B}_{ij} | \mathcal{Z}_{ij}^k = 0, \mathcal{K}^k, \mathcal{U}^k) = c, \quad (7)$$

where $c = \frac{1}{c_{max} - c_{min}}$, c_{max} and c_{min} are for the range of the image values.

For the probability of a pixel conforming to the Eq. (1) given an intermediate kernel and an intermediate image, we

define it as:

$$\begin{cases} \mathcal{P}(\mathcal{Z}_{ij}^{k+1} = 1 | \mathcal{K}^k, \mathcal{U}^{k+1}) = 1 - \mathcal{P}_0 \\ \mathcal{P}(\mathcal{Z}_{ij}^{k+1} = 0 | \mathcal{K}^k, \mathcal{U}^{k+1}) = \mathcal{P}_0 \end{cases}, \quad (8)$$

where \mathcal{P}_0 accounts for the percentage of the total image pixels deviating from the linear model. Empirically, we assume that there are around zero to ten percent pixels being deviated. Note that \mathcal{P}_0 is a parameter that can be tuned according to the actual situation.

With above definitions, the pixel screening map P_{ij} can be explicitly represented as follows:

$$P_{ij}^{k+1} = \frac{\mathcal{N}((\mathcal{K}^k * \mathcal{U}^{k+1})_{ij}, \sigma^2)(1 - \mathcal{P}_0)}{\mathcal{N}((\mathcal{K}^k * \mathcal{U}^{k+1})_{ij}, \sigma^2)(1 - \mathcal{P}_0) + c\mathcal{P}_0}. \quad (9)$$

3.2. Intermediate image correction strategy

Based on the observation that the assumption Eq. (1) may be deviated during the iterative process, we propose a novel correction strategy for blind deblurring to achieve more accurate estimation. The generic form of the blind deblurring model we aim to solve is given as follows:

$$\min_{\mathcal{U}, \mathcal{K}} \|\mathcal{K} * \mathcal{U} - \mathcal{B}\|_2^2 + \mu\rho_U(\mathcal{U}) + \nu\rho_K(\mathcal{K}), \quad (10)$$

where μ and ν are two positive parameters. In this paper, we apply the widely-used l_2 -norm as $\rho_K(\cdot)$ and select the l_0 -norm for edge selection and surface-aware regularization proposed in [17] as $\rho_U(\cdot)$ due to its superiority in suppressing the unfavorable artifacts. The regularization on image is given as:

$$\rho_U(\mathcal{U}) = \|\nabla \mathcal{U}\|_0 + \gamma \sum_{i=1}^m \sum_{j=1}^n \sqrt{1 + |\nabla_{i,j} \mathcal{U}|^2}. \quad (11)$$

To derive the kernel from (10), traditional blind deblurring methods [6, 17, 21, 24, 32] will iteratively solve the following two subproblems directly:

$$\operatorname{argmin}_{\mathcal{U}} \|\mathcal{K}^k * \mathcal{U} - \mathcal{B}\|_2^2 + \mu\rho_U(\mathcal{U}), \quad (12)$$

$$\operatorname{argmin}_{\mathcal{K}} \|\mathcal{K} * \nabla \mathcal{U}^{k+1} - \nabla \mathcal{B}\|_2^2 + \nu\|\mathcal{K}\|_2^2, \quad (13)$$

where Eq. (13) is transformed from Eq. (2) as the previous work [15, 17, 24] suggest using the gradient information of the latent image will generate a more accurate and stable kernel.

For Eq. (12), the half-quadratic splitting technique [10, 31, 34] is usually applied to solve the following problem:

$$\begin{aligned} \min_{\mathcal{U}, \mathcal{V}, \mathcal{W}} & \|\mathcal{K}^k * \mathcal{U} - \mathcal{B}\|_2^2 + \alpha\|\mathcal{U} - \mathcal{V}\|^2 + \beta\|\nabla \mathcal{U} - \mathcal{W}\|^2 \\ & + \mu\gamma \sum_{i=1}^m \sum_{j=1}^n \sqrt{1 + |\nabla_{i,j} \mathcal{V}|^2} + \mu\|\mathcal{W}\|_0. \end{aligned} \quad (14)$$

Following [17], the solution to Eq. (12) can be approached by alternatively solving $\mathcal{W}, \mathcal{V}, \mathcal{U}$ subproblems in Eq. (14) as $\alpha \rightarrow \infty$ and $\beta \rightarrow \infty$. We refer the readers to [17] for the detailed description to the solutions of $\mathcal{U}, \mathcal{V}, \mathcal{W}$. As for Eq. (13), it can be solved efficiently using a fast Fourier transform (FFT).

However, the intermediate image within the traditional iterations will contain unfavorable pixels due to the error in the given kernel and further mislead the kernel estimation, albeit Eq. (11) is designed to smooth the undesirable structures. This phenomenon is presented in Fig. 2, where the artifacts become more prominent as the iteration increases. To solve this problem, we propose an image correction strategy which removes the undesirable pixels in the intermediate image by the pixel screening map P introduced before. Specifically, after obtaining the intermediate image from Eq. (12), the image will be corrected by the screening map P for kernel estimation as following:

$$\mathcal{K}^{k+1} = \operatorname{argmin}_{\mathcal{K}} \|\mathcal{K} * \nabla(P^{k+1} \circ \mathcal{U}^{k+1}) - \nabla \mathcal{B}\|_2^2 + \nu\|\mathcal{K}\|_2^2, \quad (15)$$

where \circ is the pointwise multiplication operator. The pipeline of the blind deblurring iteration using the proposed intermediate image correction strategy is also summarized in Fig. 2.

3.3. Numerical scheme

As the blind deblurring is a highly non-convex problem, we apply the coarse-to-fine scheme proposed in [4] to estimate the kernels from the coarse to fine images as other state-of-the-art methods. Specifically, we construct the image pyramid $\mathcal{B}_1, \mathcal{B}_2, \dots, \mathcal{B}_L$ by downsampling the blurry input \mathcal{B} , where \mathcal{B}_1 equals to \mathcal{B} and \mathcal{B}_L is the coarsest blurry image downsampled by the largest factor. The computation of kernel and intermediate image will start from the coarsest level L . At each level l , \mathcal{B}_l is regarded as the blurry input \mathcal{B} of Eq. (10) in the l -th iteration, \mathcal{K}_l^0 will be the initialization of \mathcal{K} for the iteration (12), which is upsampled from $\mathcal{K}_{l-1}^{N_{max}}$ calculated in the last iteration of last level. The algorithm of proposed blind deblurring iteration is summarized in Algorithm 1.

Algorithm 1 blind deblurring using intermediate image correction

input: blurry image \mathcal{B}_l , initial kernel \mathcal{K}_l^0 , parameters $\mu, \gamma, \sigma, \mathcal{P}_0$.
for each $i \leftarrow 1, N_{max}$ **do**
 Estimate \mathcal{U}_l^i by minimizing Eq. (14),
 Compute pixel screening map P by Eq. (9),
 Compute kernel \mathcal{K}_l^i by calculating Eq. (15).
end for
output: intermediate image \mathcal{U}_l and blur kernel \mathcal{K}_l .

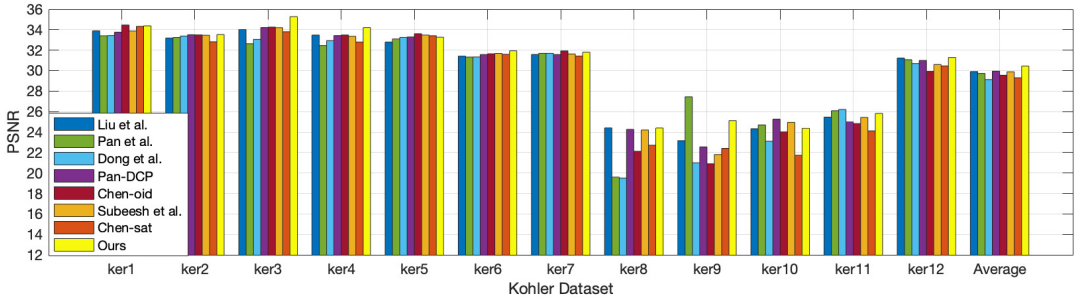


Figure 3. Quantitative performance comparison on Köhler dataset, the proposed method achieves the highest PSNR value on average.

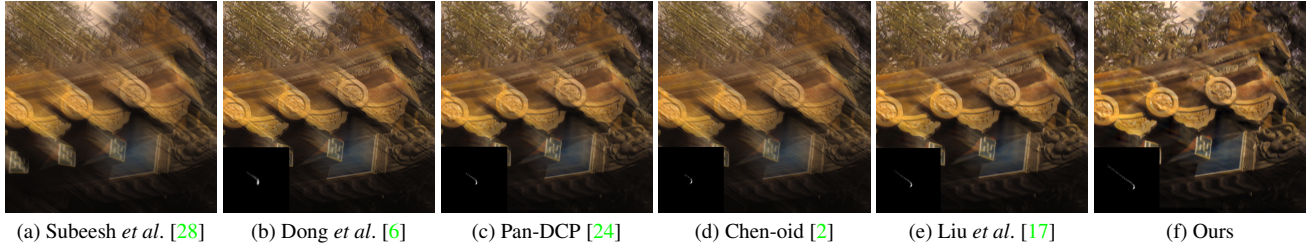


Figure 4. An example of Köhler dataset to show the effectivity of our method, compared with state-of-the-art method, our method obtain the most sharp image.

4. Experimental performance

In this section, we first evaluate the effectiveness of the proposed method on common benchmarks [12, 16] by comparing it with other state-of-the-art blind deblurring methods. Furthermore, we prove the superiority of the proposed method on the challenging datasets [14] which contain the large kernels and saturation. Finally, we evaluate the method on the real-world blurry images.

The experiments are implemented on the MATLAB platform on a PC with Intel Core i7-10700 CPU and 16.0 GB RAM. For the parameters in this work, we fix $\mu = 0.004$, $\gamma = 1$ and $\sigma = 5/255$. For the selection of the parameter \mathcal{P}_0 , we empirically find that the algorithm performs stably with \mathcal{P}_0 within $[0.01, 0.12]$ and best at 0.1 in general. For images with large saturations, a large value such as 0.12 will be suggested. Throughout our experiments, we fixed \mathcal{P}_0 as 0.1 unless specified.

The compared methods throughout the experiments include [4, 6, 17, 19, 22–24, 34, 35]. For a fair comparison, we give priority to present the deblurred results which are also published by the compared works. For those not published, we produced them by running their published codes and tried our best to reach the numerical results as reported in their paper. Moreover, we perform the non-blind deblurring [5] for synthetic datasets and [33] for real-world saturated images to get the final deblurred results unless specified. For more comparison results, we refer the readers to

the supplementary material.

4.1. Köhler *et al.* dataset

We use the Köhler dataset [12] which contains 4 images and 12 kernels to compare our method with several state-of-the-art blind deblurring methods, including [23], [6], [24], [28], [17], [2] and [3]. We selected Peak signal-to-noise ratio (PSNR) and the Structural Similarity Index (SSIM) as the metrics, where higher PSNR, SSIM values indicate the better deblurred results.

As shown in Fig. 3, our method achieves the highest PSNR consistently on the whole datasets. The average SSIM in Tab. 1 also show that our method achieves best numerical results on Köhler dataset. Additionally, the visual comparisons are conducted to prove the performance of our method. From the example illustrated in Fig. 4, one can see that other methods either fall into the initialization kernel which derives a blurry image or get an inexact kernel which derived a deblurred image with many ringing artifacts. Differently, our method gets the most accurate and sharp kernel in both cases, with which the deblurred image recovers most textures with least ringing artifacts.

4.2. Levin *et al.* dataset

We further evaluate our method on Levin *et al.* dataset [16] which contains 4 images and 8 kernels. We compare the proposed strategy with state-of-the-art algorithms, including [2, 4, 13, 15, 23–25, 27, 34], where [27] is a DL-

Table 1. Comparison of averaged SSIM on the Köhler dataset

	Pan <i>et al.</i> [23]	Dong <i>et al.</i> [6]	Pan-DCP [24]	Subeesh <i>et al.</i> [28]	Liu <i>et al.</i> [17]	Chen-oid [2]	Chen-sat [3]	Ours
SSIM	0.8757	0.8646	0.8853	0.8798	0.8786	0.8677	0.8667	0.8867

Table 2. Comparison of averaged SSIM on Levin dataset

	Krishnan <i>et al.</i> [13]	Cho&Lee [4]	Xu&Jia [34]	Levin <i>et al.</i> [15]	Pan <i>et al.</i> [23]	Pan-DCP [24]	Chen-oid [2]	Self-deblur [27]	Ours
SSIM	0.8667	0.8966	0.9174	0.9148	0.9291	0.9284	0.9146	0.9313	0.9368

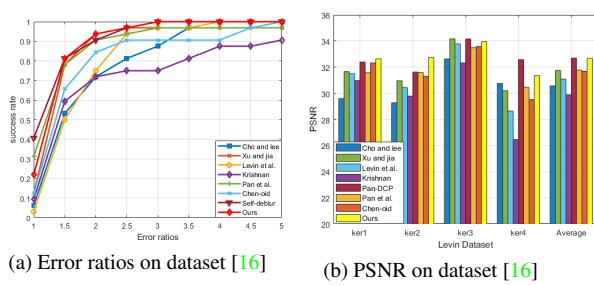


Figure 5. Quantitative evaluation on Levin’s dataset [16]. (a) is the comparison of error ratios, (b) is comparison of PSNR values.

based method which behaves relatively well among the DL-based methods. As the Error Ratio and PSNR depicted in Fig. 5 (a) and (b), our method has competitive performance against state-of-the-art methods, including deep learning method. A visual performance is presented in Fig. 6, our method obtains the kernel closest to the groundtruth kernel and reaches the highest PSNR compared with others. The PSNR values of the whole dataset depicted in Fig. 5 (b) with the average SSIM listed in Tab. 2 also prove the consistent superiority of our method.

4.3. Challenging cases

To prove the superiority of our method on challenging images, we evaluate the method on the dataset constructed by Lai [14], which contains 100 images synthesized from four large kernels and 25 images. We compare our method to the state-of-the-art methods including [2, 3, 17, 19, 20, 24, 26, 27, 35]. From the comparisons in Fig. 7 and Tab. 3, we can see that our method surpasses other methods by a large margin in the averaged numerical results. We also illustrate one example in Fig. 8 to show the visual comparison where the deblurred saturated image by our method has less ringing artifacts and higher visualization quality. More visual comparisons can be found in Sec. 2 of the supplementary materials.

4.4. Real-world images

We further evaluate our method on images obtained from real-world scenes. Fig. 9 shows two challenging cases. As one can see, for low-light images, our method derives the

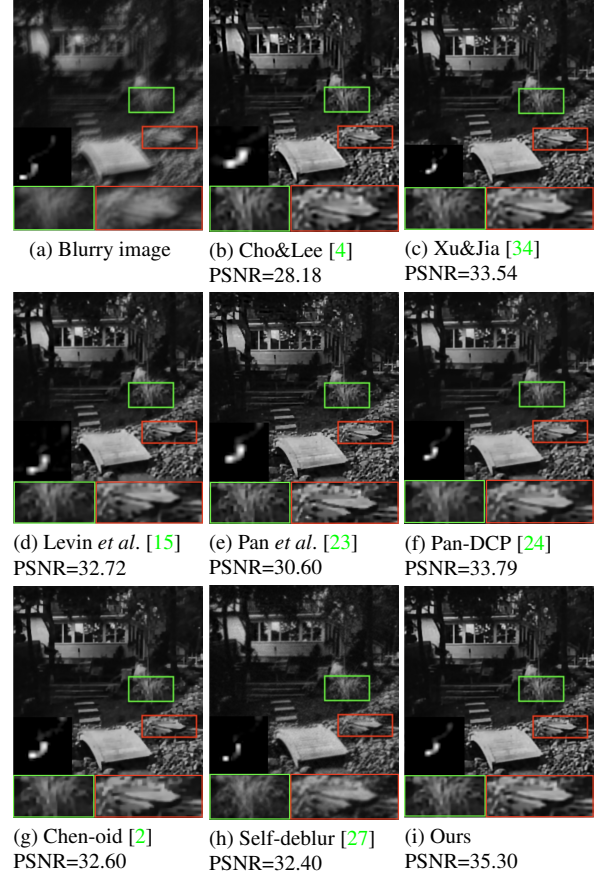


Figure 6. An example of Levin *et al.* dataset.

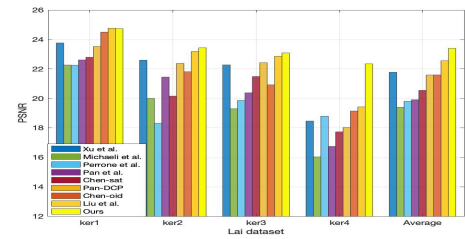


Figure 7. PSNR comparison on Lai *et al.*’s dataset.

Table 3. Comparisons of averaged SSIM on Lai *et al.*'s dataset

	Perrone <i>et al.</i> [26]	Pan <i>et al.</i> [21]	Pan-DCP [24]	Liu <i>et al.</i> [17]	Chen-oid [2]	Chen-sat [3]	Self-deblur [27]	Ours
SSIM	0.6988	0.7194	0.7462	0.7979	0.7392	0.6839	0.7525	0.8404

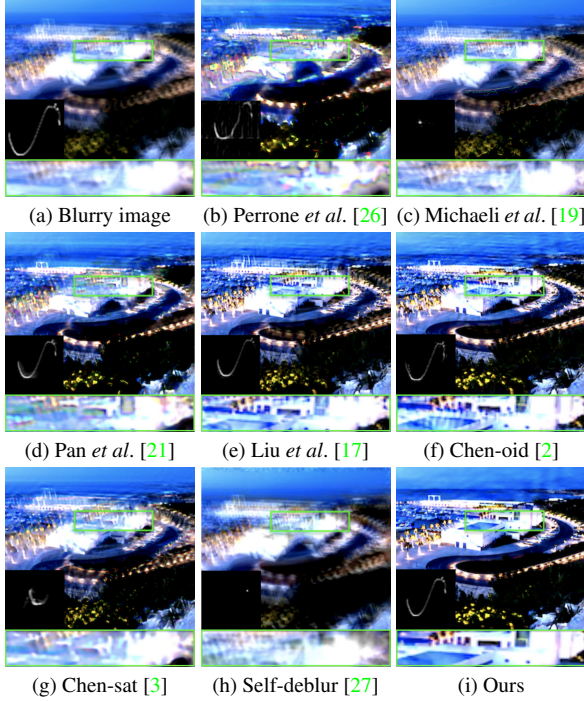


Figure 8. A saturated example of Lai *et al.* dataset.

kernels most successfully. For the face image which contains fewer edges, our method can recover most textures. More examples can be found in supplementary materials.

5. Analysis and discussion

In this section, we first analyse the effectiveness of our method in locating the deviated pixels and correcting the intermediate images. Furthermore, we analyse the differences between the existing methods and ours and further apply the intermediate correction method to these methods to demonstrate its effectiveness.

5.1. Effectiveness of the proposed strategy

To verify the effectiveness of the proposed image correction step, we compare the proposed method with the one disabling the correction step, which reduces to [17]. As seen from Fig. 10, the corrected intermediate images regularized by the surface-aware regularizations [17] are not able to recover a satisfactory blur kernel, as the estimated blur kernel stays at the identity map with the step increasing. Using this kernel for non-blind deconvolution, the final result in Fig. 10 (b) is as the input blurry image. Contrarily,

the intermediate images of the proposed method in Fig. 10 (f) prompt the kernel away from the identity position by removing the disadvantageous structures as labeled by red pixels in (f) and derive a sharp images finally. More specifically, we illustrate the pixel screening map P calculated from the images containing the outliers and ringing artifacts in Fig. 11. We could see the proposed method help locate and exclude outliers and artifacts for images and hence prompt the kernel away from the identity position.

5.2. Comparison to other methods

We compare the proposed method to the existing blind deblurring works, which are divided into three categories.

Prior based methods. Compared to most blind deblurring methods which proposed delicate priors to retrieve a more favorable intermediate images with useful information [1, 17, 22, 24], our key idea is to remove the undesirable structures from the latent image.

Edge selection based methods. For more accurate kernel estimation, some methods proposed to retrieve the most useful edge information [7, 23, 38]. [7] and [38] introduced a variable as the salient edge selection mask in their energy functions and optimize it iteratively. [23] applied the shock filters to the intermediate image and derived the salient edges through the energy function. These methods however may lead to the failure of kernel estimation as a result of insufficient details in the images where edge information is little, as shown in Fig. 3, 11 in supplementary materials.

Outlier processing methods. Many efforts have been put into dealing with the outliers in images [2, 3, 6, 8]. [6] proposed a sophisticated fidelity term to reduce the influence of the outliers to the function, however making it less sensitive to the inexact kernels. Both [2] and [8] adopt a confidence map to remove the outliers from the calculation of fidelity term and derive this map based on different sparsity priors. Hence, the performance of these methods rely heavily on the conformation of the image to the designed priors. [3] proposed a more simple and efficient way to directly shrinkage the outlier by multiplying with its inverse value. However this method overlooks the influence from the deviations below the linear model. Also, they all use the map as a weight for calculating the fidelity term, while ours uses the map to remove the any undesirable pixels inncluding the outliers before kernel estimation.

Relation to [5]. Adopting the posterior for the possibility of outliers introduced in [5] as our confidence map, we locate the deviated pixels given the intermediate \mathcal{K} and \mathcal{U} . Different from [5], we use this map to remove the deviated

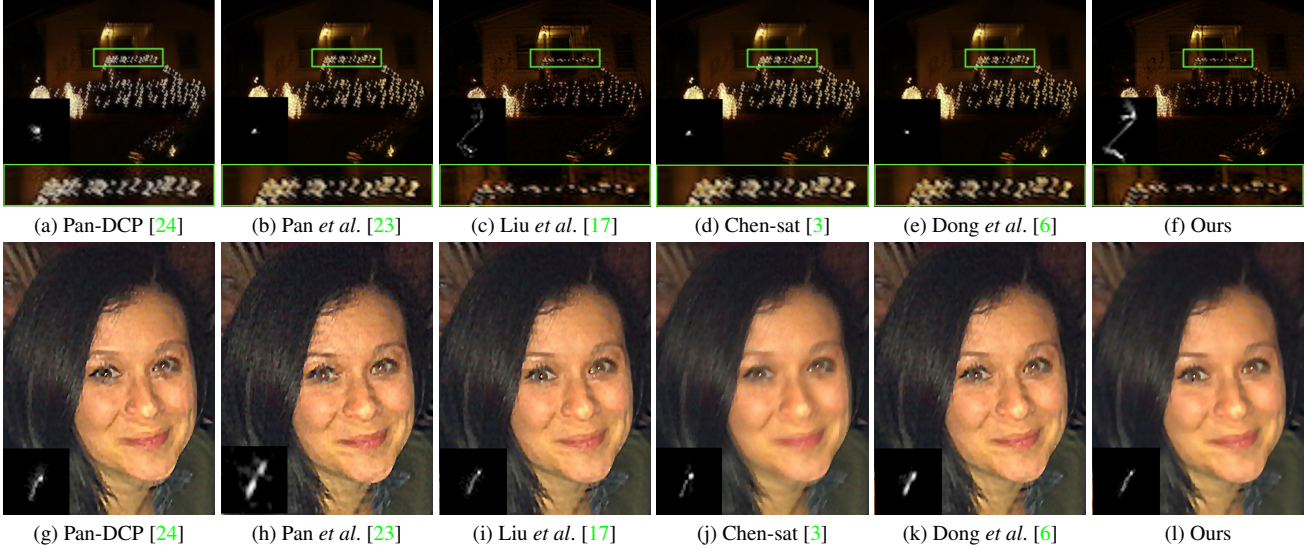


Figure 9. Two examples of real-world dataset. Our method recovers the most clear result compared with state-of-the-art methods.

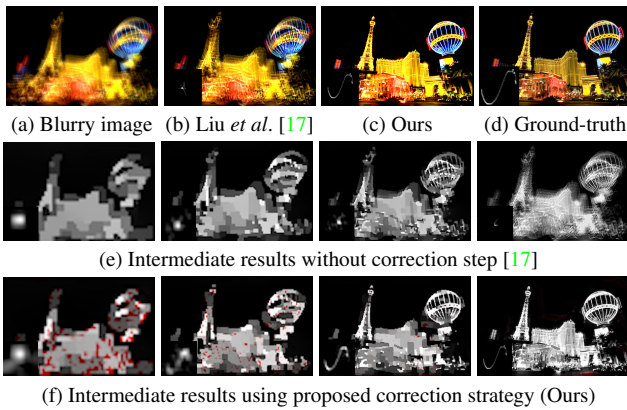


Figure 10. Comparison of deblurring iterations of the proposed model with and without the intermediate correction.

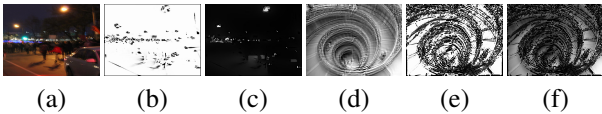


Figure 11. (a, d): the blurry images, (b, e): pixel screening masks, (c, f): corrected intermediate images.

pixels after deriving the intermediate image while [5] uses it as a weight in the fidelity term for estimating better intermediate images. Our method proves to be an effective post-processing method for blind deblurring.

5.3. Extension to other methods

As a post-processing method, it can be flexibly applied to improve different blind deblurring schemes. We have ap-

plied them on the above mentioned works [1–3, 6, 23, 24] using the same settings as given in their papers. Please refer to Sec. 5 of supplementary materials for the comparisons with and without the proposed intermediate image correction strategy. The methods adopting our method prove to reach the most stable and promising performance in the images with or without the outliers.

6. Conclusion

This paper proposes a post-processing method to correct the intermediate images for better kernel estimation, considering the importance of intermediate images for kernel estimation. By calculating the pixel screening map, our method is able to get rid of the unnecessary pixels and prompts the estimated kernel to get away from the identity position. Extensive experiments show that our method is stable, effective and reaches state-of-the-art performance combining with different deblurring schemes.

Acknowledgement.

This work was partially supported by the National Key R&D Program of China under Grant 2021YFE0203700, Grant NSFC (No.11871113, 12171049, 11171154, 11671050, 11771055, 11771053), NSFC/RGC N_CUHK 41519, Grant ITF MHP03820, Grant RGC 14300219, 14302920, 14301121, Grant CRF 8730063 and CUHK Direct Grant for Research under Grant 4053405, 4053460. We would also like to thank our team member, Hao Zhang, for sharing us with the reproduced codes of several encrypted works for extension. Finally, we would like to thank reviewers and Area Chair for their careful work and professional advice.

References

- [1] L. Chen, F. Fang, T. Wang, and G. Zhang. Blind image deblurring with local maximum gradient prior. *CVPR*, pages 1742–1750, 2019. [1](#), [2](#), [7](#), [8](#)
- [2] L. Chen, F. Fang, J. Zhang, J. Liu, and G. Zhang. OID: Outlier identifying and discarding in blind image deblurring. *ECCV*, pages 598–613, 2020. [5](#), [6](#), [7](#), [8](#)
- [3] L. Chen, J. Zhang, S. Lin, F. Fang, and J. Ren. Blind deblurring for saturated images. *CVPR*, pages 6308–6316, June 2021. [5](#), [6](#), [7](#), [8](#)
- [4] S. Cho and S. Lee. Fast motion deblurring. *ACM TOG*, 28(5):1–8, 2009. [2](#), [4](#), [5](#), [6](#)
- [5] S. Cho, J. Wang, and S. Lee. Handling outliers in non-blind image deconvolution. *ICCV*, pages 495–502, 2011. [1](#), [3](#), [5](#), [7](#), [8](#)
- [6] J. Dong, J. Pan, Z. Su, and M. Yang. Blind image deblurring with outlier handling. *ICCV*, pages 2497–2505, 2017. [4](#), [5](#), [6](#), [7](#), [8](#)
- [7] D. Gong, M. Tan, Y. Zhang, A. V. H, and Q. Shi. Blind image deconvolution by automatic gradient activation. In *CVPR*, pages 1827–1836, 2016. [7](#)
- [8] D. Gong, M. Tan, Y. Zhang, A. V. H, and Q. Shi. Self-paced kernel estimation for robust blind image deblurring. In *CVPR*, pages 1661–1670, 2017. [7](#)
- [9] Z. Hu, S. Cho, J. Wang, and M. Yang. Deblurring low-light images with light streaks. *CVPR*, pages 3382–3389, 2014. [1](#)
- [10] Y. Huang, M. K. Ng, and Y. W. Wen. A fast total variation minimization method for image restoration. *Multiscale Modeling & Simulation*, 7(2):774–795, 2008. [4](#)
- [11] N. Joshi, R. Szeliski, and D. J. Kriegman. Psf estimation using sharp edge prediction. *CVPR*, page 1–8, 2008. [2](#)
- [12] R. Köhler, M. Hirsch, B. Mohler, B. Scholkopf, and S. Harmeling. Recording and playback of camera shake: Benchmarking blind deconvolution with a real-world database. *ECCV*, pages 27–40, 2012. [2](#), [5](#)
- [13] D. Krishnan, T. Tay, and R. Fergus. Blind deconvolution using a normalized sparsity measure. *CVPR*, pages 233–240, 2011. [5](#), [6](#)
- [14] W. S. Lai, J. B. Huang, Z. Hu, N. Ahuja, and M. H. Yang. A comparative study for single image blind deblurring. *CVPR*, pages 1701–1709, 2016. [2](#), [5](#), [6](#)
- [15] A. Levin, Y. Weiss, F. Durand, and W. T. Freeman. Efficient marginal likelihood optimization in blind deconvolution. *CVPR*, pages 2657–2664, 2011. [4](#), [5](#), [6](#)
- [16] A. Levin, Y. Weiss, F. Durand, and W. T. Freeman. Understanding blind deconvolution algorithms. *IEEE TPAMI*, 33(12):2354–2367, 2011. [2](#), [5](#), [6](#)
- [17] J. Liu, M. Yan, and T. Zeng. Surface-aware blind image deblurring. *IEEE TPAMI*, 43(3):1041–1055, 2021. [1](#), [2](#), [3](#), [4](#), [5](#), [6](#), [7](#), [8](#)
- [18] Y. Liu, W. Dong, D. Gong, L. Zhang, and Q. Shi. Deblurring natural image using super-gaussian fields. In *ECCV*, September 2018. [2](#)
- [19] T. Michaeli and M. Irani. Blind deblurring using internal patch recurrence. *ECCV*, pages 783–798, 2014. [5](#), [6](#), [7](#)
- [20] J. Pan, Z. Hu, Z. Su, and M. Yang. Deblurring face images with exemplars. *ECCV*, pages 47–62, 2014. [6](#)
- [21] J. Pan, Z. Hu, Z. Su, and M. Yang. Deblurring text images via l0-regularized intensity and gradient prior. *CVPR*, pages 2901–2908, 2014. [1](#), [2](#), [4](#), [7](#)
- [22] J. Pan, Z. Hu, Z. Su, and M. H. Yang. L0-regularized intensity and gradient prior for deblurring text images and beyond. *IEEE TPAMI*, 39(2):342–355, 2017. [1](#), [2](#), [5](#), [7](#)
- [23] J. Pan, Z. Lin, Z. Su, and M. Yang. Robust kernel estimation with outliers handling for image deblurring. *CVPR*, pages 2800–2808, 2016. [5](#), [6](#), [7](#), [8](#)
- [24] J. Pan, D. Sun, H. Pfister, and M. H. Yang. Blind image deblurring using dark channel prior. *CVPR*, page 1628–1636, 2016. [1](#), [2](#), [4](#), [5](#), [6](#), [7](#), [8](#)
- [25] L. Pan, R. Hartley, M. Liu, and Y. Dai. Phase-only image based kernel estimation for single image blind deblurring. In *CVPR*, pages 6034–6043, 2019. [5](#)
- [26] D. Perrone and P. Favaro. Total variation blind deconvolution: The devil is in the details. *CVPR*, pages 2909–2916, 2014. [6](#), [7](#)
- [27] D. Ren, K. Zhang, Q. Wang, Q. Hu, and W. Zuo. Neural blind deconvolution using deep priors. *CVPR*, pages 3338–3347, 2020. [2](#), [5](#), [6](#), [7](#)
- [28] V. Subeesh and A. N. Rajagopalan. From local to global: Edge profiles to camera motion in blurred images. In *CVPR*, pages 558–567, 2017. [5](#), [6](#)
- [29] P. Tran, A. Tran, Q. Phung, and M. Hoai. Explore image deblurring via encoded blur kernel space. *CVPR*, 2021. [2](#)
- [30] D. Ulyanov, A. Vedaldi, and V. Lempitsky. Deep image prior. *CVPR*, 2018. [2](#)
- [31] Y. Wang, J. Yang, W. Yin, and Y. Zhang. A new alternating minimization algorithm for total variation image reconstruction. *SIAM Journal on Imaging Science*, 1(3):248–272, 2008. [4](#)
- [32] F. Wen, R. Ying, Y. Liu, P. Liu, and T. Truong. A simple local minimal intensity prior and an improved algorithm for blind image deblurring. *IEEE Transactions on Circuits and Systems for Video Technology*, 31(8):2923–2937, 2021. [2](#), [4](#)
- [33] O. Whyte, J. Sivic, and A. Zisserman. Deblurring shaken and partially saturated images. In *ICCV*, pages 745–752, 2011. [1](#), [5](#)
- [34] L. Xu and J. Jia. Two-phase kernel estimation for robust motion deblurring. *ECCV*, pages 157–170, 2010. [2](#), [4](#), [5](#), [6](#)
- [35] L. Xu, S. Zheng, and J. Jia. Unnatural L0 sparse representation for natural image deblurring. *CVPR*, pages 1107–1114, 2013. [2](#), [5](#), [6](#)
- [36] Z. Xu, H. Chen, and Z. Li. Fast blind deconvolution using a deeper sparse patch-wise maximum gradient prior. *Signal Processing: Image Communication*, 90:116050, 2021. [2](#)
- [37] Y. Yan, W. Ren, Y. Guo, R. Wang, and X. Cao. Image deblurring via extreme channels prior. *CVPR*, pages 6978–6986, 2017. [1](#)
- [38] L. Yang and H. Ji. A variational em framework with adaptive edge selection for blind motion deblurring. In *CVPR*, pages 10159–10168, 2019. [2](#), [7](#)
- [39] S. W. Zamir, A. Arora, S. Khan, M. Hayat, F. S. Khan, M. Yang, and L. Shao. Multi-stage progressive image restoration. In *CVPR*, 2021. [2](#)